# Automatic Impedance Matching With Dual Time-Scale P&O in Fully Self-Powered Electromagnetic Vibration Energy Harvesting

Hongfei Xiao, *Student Member, IEEE*, Han Peng, *Senior Member, IEEE*, Hanyi Sun, Yidong Zhao, Xianchao Liu, and Cheng Jiang

***Abstract*—Most of electromagnetic vibration energy harvester (EVEH) systems are only focused on resistance matching at resonant frequency. However, the EVEH will have complex output impedance at nonresonant frequencies. Pure resistance matching cannot fully extract the maximum power at nonresonance. This article is the first to propose an automatic and fully self-powered complex impedance matching EVEH system. The characteristics of the output impedance of the EVEH are analyzed, and it is found that the impedance will be distributed on a circle. An impedance-circle-based perturb-and-observe (P&O) method with dual time-scale is proposed. It perturbs the central angle with a short time-scale for fast response to vibration frequency change, and perturbs both angle and diameter with a long time scale to adapt to the slow aging and wear-out of the EVEH. Such dual time-scale P&O improves the speed and accuracy of complex impedance determination. Besides, a fully self-powered milliwatts impedance control scheme with an inductor-less H-bridge ac–dc converter is designed. Experiments show that the designed system can realize complex impedance matching control stably and quickly. The maximum improvement of the output power of the converter reaches 25% compared to resistance matching scheme at nonresonant frequencies. Under the excitation acceleration amplitude of 3 m/s$^2$ at the resonant frequency, the system generates the maximum power of 10.11 mW with the overall system efficiency reaching 82.2%. It is the first time the automatic complex impedance matching is realized in millipower fully self-powered EVEH.**

***Index Terms*—AC–DC converter, automatic complex impedance matching, dual time-scale, electromagnetic vibration energy harvester, perturb and observe.**

## I. INTRODUCTION

THE goal of energy harvesting is to replace batteries or extend the recharge intervals of batteries for widely distributed wireless sensors in Internet of Things [1], [2]. Electromagnetic vibration energy harvester (EVEH) generates energy through the vibration-induced relative movement between the coil and permanent magnet [3]. It has proven to be efficient and high power density [4].

The ac power generated by the EVEH needs to be converted into dc power to supply loads. To maximize the power delivery, input characteristic of the ac–dc converter should be controlled to match with the output characteristic of the EVEH [5]. EVEHs are usually designed to work at resonant frequency to increase the output power. When the ambient vibration frequency is exactly equal to the resonant frequency, the output impedance of the EVEH is purely resistive. Majority of prior arts have focused on resistive matching, such as using rectifier with dc–dc converter [6], [7] or direct ac–dc converter [8], [9], [10], [11] to match a resistive load. The resistance value can be determined by methods such as perturb-and-observe (P&O) [11], [12] or fractional open-circuit voltage (FOCV) [6] method in these converters. In short, the impedance matching scheme is relatively mature and has achieved high efficiency at resonance.

However, the frequency of ambient vibration cannot always be exactly the same as the resonant frequency of the EVEH. At nonresonant frequencies, the EVEH will present complex impedance characteristics. The output power of the EVEH will drop significantly even if the frequency deviates slightly from the resonance, which limits the operating frequency bandwidth of the EVEH. In [13], a general impedance model was given to explain the need for counteracting the effect of the output reactance. In order to operate the harvester at the true maximum power point, the load impedance should be equal to the complex conjugate of the output impedance of the source [14]. Experimental implementation and validation of using passive inductors and capacitors to increase the output power of the EVEH have been reported in [15] and [16]. But the flexibility of using passive components was poor and could not adapt to frequency changes.

It is more feasible to synthesize a complex load impedance by using a four-quadrant ac–dc converter. In [17], [18], and [19], complex impedance was realized by an H-bridge ac–dc converter and a phase-shifted current reference. However, complex

Manuscript received 5 June 2023; revised 27 August 2023; accepted 14 October 2023. Date of publication 25 October 2023; date of current version 26 January 2024. This work was supported by the State Grid Corporation of China (SGCC) under Project 52094020006X. Recommended for publication by Associate Editor K. Kim. *(Corresponding author: Han Peng.)*

Hongfei Xiao, Han Peng, Yidong Zhao, Xianchao Liu, and Cheng Jiang are with the State Key Laboratory of Advanced Electromagnetic Technology (AET), School of Electrical and Electronic Engineering, Huazhong University of Science and Technology, Wuhan 430074, China (e-mail: d202080611@hust.edu.cn; misspenghan@163.com; m202271933@hust.edu.cn; m202071547@hust.edu.cn; cheng_jiang@hust.edu.cn).

Hanyi Sun is with the China-EU Institute for Clean and Renewable Energy, Huazhong University of Science and Technology, Wuhan 430074, China (e-mail: sunhy@hust.edu.cn).

Color versions of one or more figures in this article are available at https://doi.org/10.1109/TPEL.2023.3327458.

Digital Identifier 10.1109/TPEL.2023.3327458

impedance was given in advance in these works, which also cannot adapt to frequency changes automatically.

In [20], an automatic impedance matching method based on the dual-variable P&O algorithm was proposed. It alternately perturbed the amplitude and phase of reference signal, and determined the matching impedance by observing the output power of the converter. To improve the speed of the determination process of reference signal, a dual-variable overturn and observe (O&O) method was proposed in [21]. In [22] and [23], another dual-variable method was also proposed to determine the impedance. The coil reactance was determined by observing the critical stable state of the impedance controller, and the resistance was still determined by P&O. Two parameters were needed to be determined in the aforementioned works to adapt to frequency changes, which resulted in slow response speed.

In addition, prior complex impedance matching systems usually required a continuously worked microcontroller unit (MCU) to generate reference signals [19], or pulsewidth modulation (PWM) signals [20], [21], [23]. Currently, low-power MCUs that continuously execute sampling, calculation, and output require at least several hundred microwatts to several milliwatts of power consumption [24], [25], which is hard to undertake by a millipower EVEH.

At present, there is no work that has realized automatic impedance matching in a fully self-powered millipower EVEH. This article proposes a novel automatic and fully self-powered complex impedance matching system to enhance the power delivery of the EVEH at nonresonance. The main contributions of this work can be summarized as follows.

1) The output impedance of the EVEH under different frequencies is analyzed. It is pointed out that the impedance will be distributed on a circle. The change in vibration frequency corresponds to the change in source central angle ($\varphi_S$), and the slow aging and wear-out of mechanical components correspond to the change in diameter.
2) An impedance circle-based P&O method that perturbs the central angle and diameter with dual time-scale is proposed to determine the complex impedance of the EVEH. The load central angle ($\varphi_L$) is the only variable that needs to be perturbed in most of time. The reduction of the number of variables to be perturbed improves the speed and accuracy of complex impedance determination.
3) Self-powered and automatic impedance matching are applied in the EVEH system for the first time, improving the output power of the EVEH at nonresonance effectively. A series of low-power consumption design schemes are proposed that enable automatic impedance matching to be truly applied in the millipower EVEH system.

The rest of this article is organized as follows. Section II illustrates the output characteristics of the EVEH and the proposed dual time-scale P&O method. Section III describes the impedance control strategy. Section IV shows the system structure and the circuit implementation of a fully self-powered and automatic impedance matching system. Section V shows the designed compact EVEH prototype and the measurement results. Finally, Section VI concludes this article.

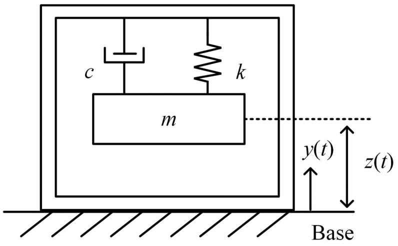

Fig. 1. Lumped element model of the spring–mass–damper system.

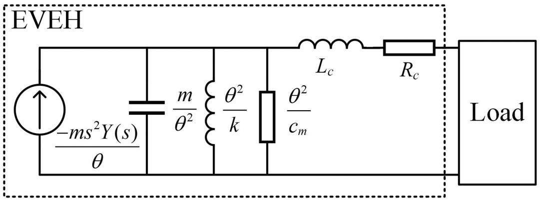

Fig. 2. Equivalent circuit model of the EVEH.

## II. Output Characteristics of the EVEH and Impedance Matching Method

### A. Equivalent Circuit and Output Impedance of the EVEH

The EVEH can be modeled as a base excited, second-order, linear spring–mass–damper system. The lumped element model of the EVEH is presented in Fig. 1. The Laplace transform equation of motion can be described as

$$ms^2Z(s) + csZ(s) + kZ(s) = -ms^2Y(s) \tag{1}$$

where $m$ is mass suspended on the spring, $c$ is viscous damping coefficient, $k$ is spring constant, and $Y$ and $Z$ are absolute vibration displacement of base and relative displacement between coil and magnet, respectively. Damping of the system is composed of mechanical damping and electromagnetic damping as [26]

$$c = c_m + \frac{\theta^2}{R_c + R_{\text{load}}} \tag{2}$$

where $c_m$ is mechanical damping coefficient, $\theta$ is electromechanical coupling coefficient, and $R_c$ and $R_{\text{load}}$ are coil resistance and load resistance, respectively. According to (1), the equivalent circuit model of the EVEH can be established as shown in Fig. 2 [27]. Vibration of the base can be considered as a current source. The mechanical parameters are modeled as paralleled capacitor, inductor, and resistor.

Suppose the vibration frequency is $\omega$, the total output impedance of the EVEH ($Z_{\text{EH}}$) can be expressed as

$$Z_{\text{EH}} = \frac{j\omega\theta^2}{k - \omega^2 m + j\omega c_m} + R_c + j\omega L_c \tag{3}$$

where $L_c$ is the coil inductance. According to (3), the real part of the output impedance is

$$\text{Re} = \frac{c_m\omega^2\theta^2}{(k-\omega^2 m)^2 + c_m^2\omega^2} + R_c. \tag{4}$$

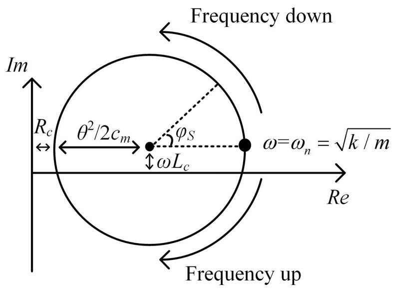

Fig. 3. Circular distributed impedance of the EVEH.

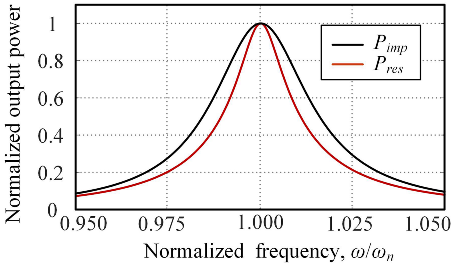

Fig. 4. Output power comparisons of impedance matching and resistance matching at different frequencies.

And the imaginary part is

$$\mathrm{Im} = \frac{\omega\theta^2(k-\omega^2 m)}{(k-\omega^2 m)^2 + c_m^2\omega^2} + \omega L_c. \quad (5)$$

It can be found that the real part and imaginary part are distributed on a circle with center at ($R_c + \theta^2/2c_m$, $\omega L_c$) and diameter of $\theta^2/c_m$. Define the mechanical damping equivalent resistance ($\theta^2/c_m$) as $R_m$, the impedance circle can be described as

$$(\mathrm{Im} - \omega L_c)^2 + \left(\mathrm{Re} - \frac{R_m}{2} - R_c\right)^2 = \left(\frac{R_m}{2}\right)^2. \quad (6)$$

Fig. 3 shows the distribution of $Z_{\mathrm{EH}}$. Ignoring the coil reactance $\omega L_c$, the output impedance is purely resistive at resonant frequency $\omega_n$ of $\sqrt{k/m}$ [11]. In most of prior arts, only resistance matching is considered [6], [7], [8], [9], [10], [11], which results in much less harvested power at nonresonant frequencies.

Fig. 4 shows the output power comparisons of the impedance matching ($P_{\mathrm{imp}}$) and resistance matching ($P_{\mathrm{res}}$) at different frequencies, plotted under $R_m$ of 63.7 Ω and $R_c$ of 6.3 Ω. It can be seen that complex impedance matching will increase the output power of the EVEH at nonresonant frequencies.

### B. Dual Time-Scale P&O Method Based Upon Impedance Circle

P&O method is commonly adopted to realize impedance matching for maximum power point tracking. In prior arts, determining impedance required to alternately perturb two variables, for example, amplitude and phase of the reference signal [20]. It led to slow response and low accuracy. A faster and more precise P&O method is presented in this section.

As plotted in Fig. 3, the impedance of an EVEH can be expressed by source central angle $\varphi_S$ as

$$\begin{cases} \mathrm{Re} = \frac{2R_c + R_m(1+\cos\varphi_S)}{2} \\ \mathrm{Im} = \frac{R_m \sin\varphi_S}{2} + \omega L_c \end{cases}. \quad (7)$$

Thus, to determine the complex impedance of an EVEH, four parameters need to be determined: $R_c$, $\omega L_c$, $R_m$, and $\varphi_S$. Obviously, the corresponding matched load impedance will distribute on another load impedance circle with center at ($R_c + \theta^2/2c_m$, $-\omega L_c$) and diameter of $R_m$. The load central angle ($\varphi_L$) satisfies

$$\varphi_L = -\varphi_S. \quad (8)$$

The coil resistance $R_c$ and inductance $L_c$ do not vary much and can be obtained by testing in advance. In a typical small-scale EVEH, coil reactance $\omega L_c$ is much smaller than $R_c$, which can be ignored [9], [11]. Even in some cases where $\omega L_c$ cannot be ignored [12], $\omega L_c$ can be considered to be approximately equal to $\omega_n L_c$ because the resonant EVEHs usually harvest energy around the resonant frequency in a narrow bandwidth. Thus, coil resistance and reactance are parameters that can be predetermined.

The value of $R_m$ is related to $\theta$ and $c_m$. $\theta$ can be expressed as

$$\theta = NBl \quad (9)$$

where $N$ is the number of coil turns, $B$ is the average magnetic flux density in the air gap, and $l$ is the coil length across the magnetic flux. The change in $\theta$ comes only from magnet demagnetization, which is extremely slow. The change in $c_m$ is related to the aging and wear-out of mechanical structure and material [28], [29], which is also a long and slow process. Thus, the variation of $R_m$ is an extremely slow process. It is sufficient to track $R_m$ by a long time-scale P&O method.

The variation of angle $\varphi_S$ is due to vibration frequency change, which can be fast and random in practical applications. A short time-scale P&O is required to track $\varphi_S$. Thus, impedance circle-based P&O method with dual time-scale is proposed in this article: perturbing $\varphi_L$ with short time-scale to determine the frequently changed $\varphi_S$; determining $R_m$ once with a long time-scale by another dual-variable P&O [20] to adapt to slow aging and wear-out of the EVEH. In most of time, this method only perturbs $\varphi_L$ to find the optimal impedance. The reduction of the number of variables to be perturbed is beneficial to improve the speed and accuracy of impedance determination.

The following content demonstrates that the approach of perturbing $\varphi_L$ and observing the change in the output power can always find the optimal matched impedance. Assume that the currently determined $R_m$ value is $R'_m$ in the algorithm, the output power of the EVEH can be expressed as (10) shown at the bottom of the next page, where $I_{\mathrm{rms}}$ is the rms value of the current source in Fig. 2. Force the derivative with respect to $\varphi_L$ to zero to find the extremum points of output power, as

$$\frac{dP(\varphi_S, \varphi_L, R_m, R'_m)}{d\varphi_L} = 0. \quad (11)$$

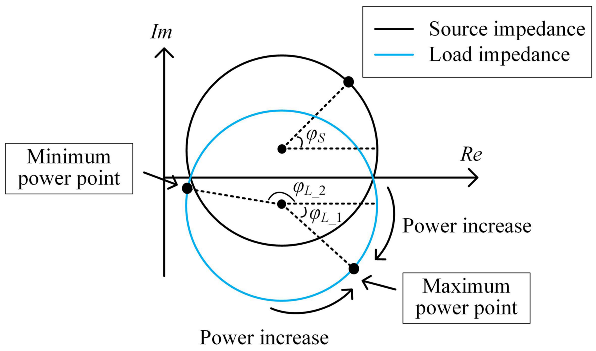

Fig. 5. Direction of power variation on the impedance circle.

When $R'_m$ is equal to $R_m$, two solutions can be obtained, as

$$\begin{cases} \varphi_{L\_1} = -\varphi_S \\ \varphi_{L\_2} = -j\ln\left(-\frac{R_m + 2R_c + R_m e^{j\varphi_S}}{R_m + (R_m + 2R_c)e^{j\varphi_S}}\right) \end{cases}. \tag{12}$$

Fig. 5 shows the location of $\varphi_{L\_1}$ and $\varphi_{L\_2}$ with the direction of power variation on the impedance circle. It shows that the output power has only a maximum value point at $\varphi_{L\_1}$, and a minimum value point at $\varphi_{L\_2}$. Thus, the P&O method of perturbing $\varphi_L$ and observing output power will always find the optimal impedance point along the power increase direction shown in Fig. 5.

The determination of $R'_m$ requires another dual-variable P&O [20] process that perturb $\varphi_L$ and $R'_m$ alternately. The fluctuated $\varphi_L$ in the determination process may lead to error of $R'_m$ because $\varphi_L$ cannot be exactly equal to $-\varphi_S$. The determined $R'_m$ by P&O can be obtained by solving

$$\frac{dP(\varphi_S, \varphi_L, R_m, R'_m)}{dR'_m} = 0. \tag{13}$$

If matching $\varphi_S$ (as $\varphi_L = -\varphi_S$) when the determined $R'_m$ deviates from $R_m$, the output power ($P'_{\max}$) can be expressed as (14) shown at the bottom of this page. Fig. 6 shows the determined $R'_m$ and $P'_{\max}/P_{\max}$ at $\varphi_S$ is 0° with $\varphi_L$ changing from −90° to 90°, where $P_{\max}$ is the maximum output power of the EVEH at $\varphi_L = -\varphi_S = 0°$ and $R'_m = R_m$. It can be seen that when $\varphi_L$ differs from $\varphi_S$ by 90°, the determined $R'_m$ by P&O will have a 37% error. However, even in such a large error of $R'_m$, $P'_{\max}$ can reach 97.6% of the optimal maximum power.

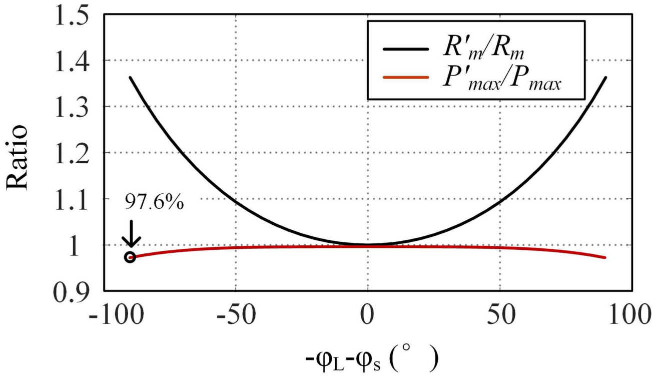

Fig. 6. Determined $R'_m$ and $P'_{\max}$ at $\varphi_S = 0°$ with $\varphi_L$ changing from −90° to 90°.

In actual applications, the fluctuation of $\varphi_L$ is much lower than 90°. This shows that the dual-variable P&O can finally obtain an accurate $R'_m$ value.

## III. IMPEDANCE CONTROLLER AND CONTROL STRATEGY

### A. Impedance Controller

To realize complex impedance matching, an impedance controller with three operation branches is proposed in this article, with block diagram shown in Fig. 7. $V_{\text{eq}}$ is the Thevenin equivalent voltage source extracted from Fig. 2. $V_{\text{EH}}$ and $I_{\text{EH}}$ are the output voltage and current of the EVEH. $V_{\text{ref}}$ is the reference signal, which is obtained through the proportional and integral, or proportional and differential operations of $I_{\text{EH}}$. Adjusting the gains of the three operation branches ($Gain_p$, $Gain_I$, and $Gain_D$) can control the phase and amplitude of $V_{\text{ref}}$, and then, control the equivalent impedance of the ac–dc converter. When Im > 0, the EVEH is inductive. The proportional and integral operation branches are adopted to make the input impedance of the converter being capacitive. When Im ≤ 0, the EVEH is capacitive. The proportional and differential operation branches are adopted to make the input impedance of the converter being inductive.

The transfer function of $I_{\text{EH}}(s)/V_{\text{eq}}(s)$ is shown in (15) shown at the bottom of this page, where $F_{P,I,D}(s)$ represents the transfer function of the signal processing, including the signal attenuation and delay caused by filters, low gain bandwidth product

---

$$P(\varphi_S, \varphi_L, R_m, R'_m) = \frac{I_{\text{rms}}^2\left((2R_c + R_m(1+\cos\varphi_S))^2 + (R_m\sin\varphi_S)^2\right)(2R_c + R'_m(1+\cos\varphi_L))}{2\left((4R_c + R_m(1+\cos\varphi_S) + R'_m(1+\cos\varphi_L))^2 + (R_m\sin\varphi_S + R'_m\sin\varphi_L)^2\right)}. \tag{10}$$

---

$$P'_{\max} = \frac{I_{\text{rms}}^2\left((2R_c + R_m(1+\cos\varphi_S))^2 + (R_m\sin\varphi_S)^2\right)(2R_c + R'_m(1+\cos\varphi_S))}{2\left((4R_c + R_m(1+\cos\varphi_S) + R'_m(1+\cos\varphi_S))^2\right)} \tag{14}$$

$$\frac{I_{\text{EH}}(s)}{V_{\text{eq}}(s)} = \begin{cases} \frac{1}{\frac{\theta^2 s}{ms^2+c_m s+k}+R_c+L_c s+\text{Gain}_P F_P(s)+\frac{\text{Gain}_I}{s}F_I(s)}, \text{Im} > 0 \\ \frac{1}{\frac{\theta^2 s}{ms^2+c_m s+k}+R_c+L_c s+\text{Gain}_P F_P(s)+\text{Gain}_D sF_D(s)}, \text{Im} \le 0 \end{cases}. \tag{15}$$

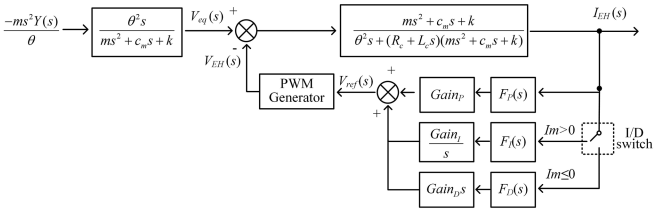

Fig. 7. Block diagram of the impedance controller.

(GBP) devices, and compensators designed for system stability. A second-order low-pass filter is necessary in signal stage to filter out large switching frequency ripple in $I_{\mathrm{EH}}$ [23]. Low-GBP operational amplifiers are used for low power consumption, but will lead to large attenuation and delay. The phase margin of the controller will also be sacrificed so that compensators are necessary to be designed. The transfer function of $F_{P,I,D}(s)$ can be expressed as

$$F_x(s) = \left.\frac{\prod_{i=1}^{z_x}(T_{xzi}s+1)}{\prod_{i=1}^{p_x}(T_{xpi}s+1)}\right|_{x=P,I,D} \tag{16}$$

where $z_x$ and $p_x$ ($x = P, I, D$) represent the total number of zeros and poles, respectively. Since the frequency corresponding to the zeros and poles of $F_x(s)$ is much higher than the vibration frequency, the high-order term can be ignored and only the first-order term is considered for vibration frequency signals. Thus, $F_x(j\omega)$ can be approximately written as

$$F_x(j\omega) \approx \left.\frac{j\omega\sigma_{xz}+1}{j\omega\sigma_{xp}+1}\right|_{x=P,I,D} \tag{17}$$

where $\sigma_{xz}$ and $\sigma_{xp}$ are the sum of the time constants on the numerator and denominator of (16).

The signal processing will affect amplitude and phase of $V_{\mathrm{ref}}$. Considering the effect of $F_{P,I,D}(j\omega)$, the matched impedance satisfies

$$\begin{cases}\mathrm{Re}-j\mathrm{Im} = \mathrm{Gain}_P F_P(j\omega) + \frac{\mathrm{Gain}_I F_I(j\omega)}{j\omega}, \mathrm{Im}>0 \\ \mathrm{Re}-j\mathrm{Im} = \mathrm{Gain}_P F_P(j\omega) + j\omega\mathrm{Gain}_D F_D(j\omega), \mathrm{Im}\leq 0\end{cases}. \tag{18}$$

The gains can be solved by combining (17) and (18). As the EVEH generally operates around the resonant frequency, $\omega$ is replaced by $\omega_n$ in the proposed controller. When $\mathrm{Im} > 0$, the solutions are (19) and (20) shown at the bottom of this page. When $\mathrm{Im} \leq 0$, the solutions are (21) and (22) shown at the bottom of this page. Equations (19)–(22) eliminate the attenuation and delay of signal processing, allowing a more accurate control of impedance. These parameters are constants that can be predetermined in the design.

## *B. Step Size and Time Interval of P&O*

The step size and time interval in $\varphi_L$ perturbation are illustrated in this section. Large step size will lead to large power fluctuations, while small step size will lead to slow response speed. In this article, variable step sizes are designed under equal power fluctuations at each $\varphi_L$ perterbation to balance power fluctuations and response speed. Suppose $\varphi_L$ is a series of angle values from $\varphi_{L(\text{-}n)}$ to $\varphi_{L(n)}$. When the optimal matched angle is $\varphi_{L(i)}$, the P&O algorithm will work in a stable trilevel condition [30]: $\varphi_{L(i-1)}, \varphi_{L(i)}$, and $\varphi_{L(i+1)}$. Power fluctuation factor ($\varepsilon_p$) is defined as

$$\varepsilon_p = \frac{\begin{array}{c}P(-\varphi_{L(i)}, \varphi_{L(i)}, R_m, R'_m) \\ -P(-\varphi_{L(i)}, \varphi_{L(i+1)}, R_m, R'_m)\end{array}}{P(0, 0, R_m, R'_m)} \tag{23}$$

where $P(0, 0, R_m, R'_m)$ is the maximum power at resonance, and $\varepsilon_p$ represents the ratio of the power fluctuation to $P(0, 0, R_m, R'_m)$ when $\varphi_S = -\varphi_L(i)$ and $\varphi_L = \varphi_{L(i+1)}$. Set the initial $\varphi_{L(0)}$ to 0°, step angles ($\varphi_{L(1)}$ to $\varphi_{L(n)}$) can be solved by iterating (23), and $\varphi_{L(\text{-n})}$ to $\varphi_{L(-1)}$ can be obtained symmetrically as: $\varphi_{L(\text{-}n)} = -\varphi_{L(n)}$. This calculation process will be done automatically in MCU once $R'_m$ is updated. Fig. 8 shows the uneven 19 step sizes on the impedance circle under $R_m$ and $R'_m$ of 63.7 Ω, $R_c$ of 6.3 Ω, and $\varepsilon_p$ of 1%.

The time interval of $\varphi_L$ perturbation is also an important parameter for the P&O algorithm. The basic requirement is that the output power should reach to steady state when it is observed, otherwise the algorithm will be unstable. The settling time of the impedance matching system includes settling time of circuit system ($t_{\mathrm{cir}}$) and mechanical system ($t_{\mathrm{mech}}$). The time interval of $\varphi_L$ perturbation needs to satisfy

$$\Delta t_{\mathrm{P\&O}} > t_{\mathrm{cir}} + t_{\mathrm{mech}}. \tag{24}$$

The circuit system includes ac–dc converter, controller, and sampling circuit. $t_{\mathrm{cir}}$ can be obtained by considering the step response of their respective transfer functions [13]. $t_{\mathrm{mech}}$ is related to the transient response of the mechanical system when

---

$$\mathrm{Gain}_P = \frac{\left(\mathrm{Re}(\sigma_{Iz}\sigma_{Ip}\omega_n^2+1) - \omega_n\mathrm{Im}(\sigma_{Iz}-\sigma_{Ip})\right)(\sigma_{Pp}^2\omega_n^2+1)}{(\sigma_{Pz}\sigma_{Pp}\omega_n^2+1)(\sigma_{Iz}\sigma_{Ip}\omega_n^2+1)+\omega_n^2(\sigma_{Pz}-\sigma_{Pp})(\sigma_{Iz}-\sigma_{Ip})}, \quad \mathrm{Im}>0 \tag{19}$$

$$\mathrm{Gain}_I = \frac{\left(\omega_n^2\mathrm{Re}(\sigma_{Pz}-\sigma_{Pp}) + \omega_n\mathrm{Im}(\sigma_{Pz}\sigma_{Pp}\omega_n^2+1)\right)(\sigma_{Ip}^2\omega_n^2+1)}{\omega_n^2(\sigma_{Pz}-\sigma_{Pp})(\sigma_{Iz}-\sigma_{Ip})+(\sigma_{Pz}\sigma_{Pp}\omega_n^2+1)(\sigma_{Iz}\sigma_{Ip}\omega_n^2+1)}, \quad \mathrm{Im}>0 \tag{20}$$

$$\mathrm{Gain}_P = \frac{\left(\mathrm{Re}(\sigma_{Dz}\sigma_{Dp}\omega_n^2+1) + \omega_n\mathrm{Im}(\sigma_{Dp}-\sigma_{Dz})\right)(\sigma_{Pp}^2\omega_n^2+1)}{(\sigma_{Pz}\sigma_{Pp}\omega^2+1)(\sigma_{Dz}\sigma_{Dp}\omega^2+1)-\omega_n^2(\sigma_{Pz}-\sigma_{Pp})(\sigma_{Dp}-\sigma_{Dz})}, \quad \mathrm{Im}\leq 0 \tag{21}$$

$$\mathrm{Gain}_D = \frac{\left(\omega_n\mathrm{Re}(\sigma_{Pz}-\sigma_{Pp}) + \mathrm{Im}(\sigma_{Pz}\sigma_{Pp}\omega_n^2+1)\right)(\sigma_{Dp}^2\omega_n^2+1)}{\omega_n^3(\sigma_{Pz}-\sigma_{Pp})(\sigma_{Dp}-\sigma_{Dz})-\omega_n(\sigma_{Pz}\sigma_{Pp}\omega_n^2+1)(\sigma_{Dz}\sigma_{Dp}\omega_n^2+1)}, \quad \mathrm{Im}\leq 0. \tag{22}$$

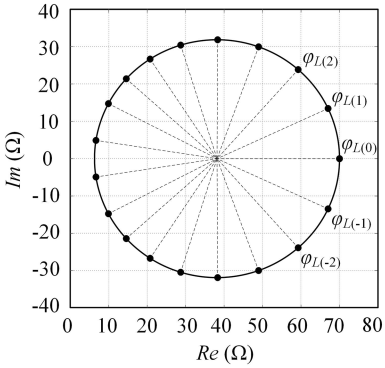

Fig. 8. Calculated step size of $\varphi_{L(-n)}$ to $\varphi_{L(n)}$ under $R_m$ of 63.7 Ω, $R_c$ of 6.3 Ω and $\varepsilon_p$ of 1%.

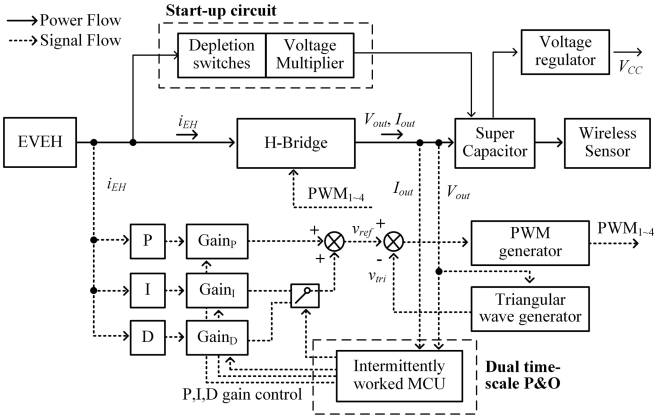

Fig. 9. Architecture of the complete self-powered and automatic impedance matching system.

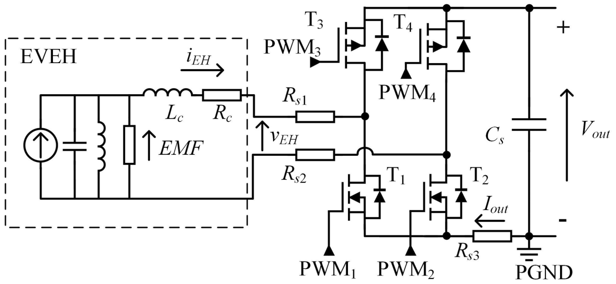

Fig. 10. H-bridge ac–dc converter adopted in this article.

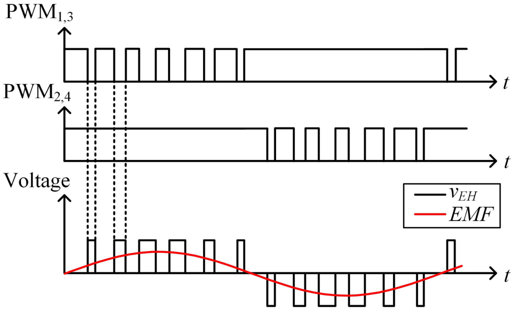

Fig. 11. Fundamental operation waveforms for the H-bridge boost AC–DC converter.

load changes. Under complex load, (1) becomes a three-order differential equation. It is difficult to accurately obtain a settling time when the complex load changes. However, the maximum $t_{\text{mech}}$ can be obtained by changing the EVEH from open-circuit to short-circuit at resonance. Therefore, the most conservative estimate of $t_{\text{mech}}$ is [11]

$$t_{\text{mech}} \leq \frac{2m}{c_m} \ln \frac{\left(1+\sqrt{1+\varepsilon_t}\right)\theta^2}{\varepsilon_t\left(R_c c_m+\theta^2\right)} \tag{25}$$

where $\varepsilon_t$ is the error of output power when the EVEH is considered to be a stable state.

## IV. CIRCUIT IMPLEMENTATION

The architecture of the complete self-powered and automatic impedance matching system is shown in Fig. 9. The main power conversion stage adopts an H-bridge ac–dc converter with load of supercapacitor. A start-up circuit with depletion switches and voltage multiplier is designed to ensure that the whole system can be completely self-powered. In order to control the equivalent input impedance of the H-bridge circuit, the voltage reference signal ($v_{\text{ref}}$) is obtained through the proportional and integral, or proportional and differential operations of the EVEH output current $i_{\text{EH}}$. $v_{\text{ref}}$ is directly compared with the triangular signal ($v_{\text{tri}}$) to obtain the PWM signal. To reduce power consumption, the sampling and operation are all realized by analog components, and the proposed P&O algorithm by impedance circle is implemented by an intermittently worked MCU.

### A. Inductor-Less AC–DC Converter and Operating Principles

The topology of the H-bridge inductor-less ac–dc converter is shown in Fig. 10, where EMF and $v_{\text{EH}}$ are the induced electromotive force and output voltage of the EVEH, respectively. The coil inductance is used as the filter inductance to improve the power density of the whole module. Two Gallium Nitride high-electron-mobility transistors (GaN HEMT) are used as low-side switches due to the ultralow total gate charge. Two P-type MOSFETs (PMOS) are used as high-side switches to avoid using isolated drivers.

The converter works in bipolar mode, with the fundamental operation waveforms shown in Fig. 11. In a positive input interval, power transistor $T_2$ is kept ON and $T_4$ is kept OFF, while $T_1$ and $T_3$ are controlled ON and OFF. Oppositely, $T_1$ is kept ON and $T_3$ is kept OFF, while $T_2$ and $T_4$ are controlled ON and OFF, respectively, in the negative input interval. The bipolar PWM has two advantages. The first is that the states of two switches are always remain unchanged in the half-vibration period, which can reduce the driving and switching losses. Second, it can cooperate with the dual-resistor sampling strategy introduced later to reduce the common-mode voltage on the differential amplifier.

The triangular wave generator and bipolar double-frequency PWM generator are shown in Fig. 12. The triangular signal is

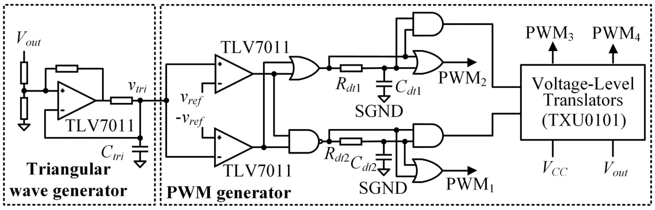

Fig. 12. Triangular wave generator and bipolar double-frequency PWM generator. All logic gates are of the SN74AUP1G series.

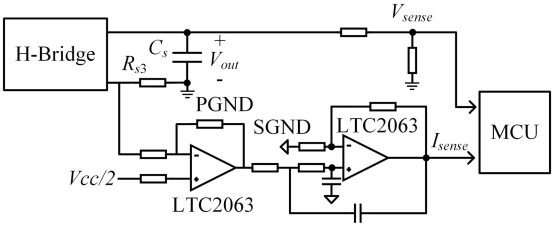

Fig. 14. Output voltage and output current sensing circuit.

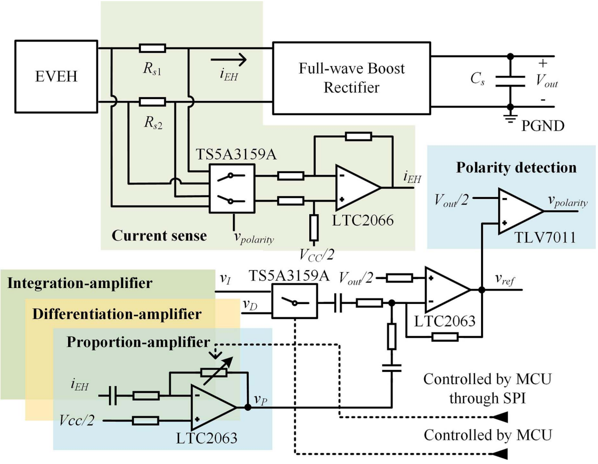

Fig. 13. Dual-resistor input current sensing circuit with proportional, integral, and differential operation circuit.

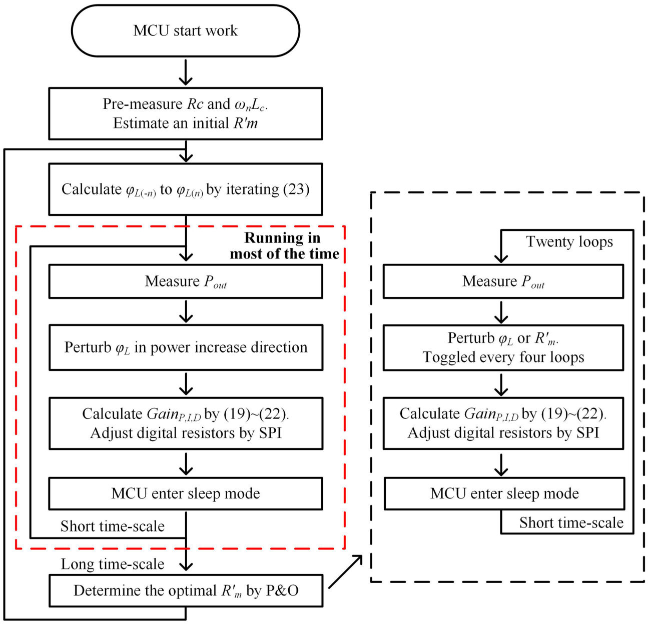

Fig. 15. Flowchart of the proposed impedance circle-based P&O with dual time-scale.

generated by periodically charging and discharging the capacitor ($C_{\text{tri}}$) through the comparator (TLV7011). By comparing $v_{\text{tri}}$ with the positive and negative $v_{\text{ref}}$, PWM signals at twice frequency of the triangular wave are generated, which can reduce the dynamic power loss of the comparator in the triangular wave generator. Voltage translators are used for level shifting to increase the voltage level of PMW$_3$ and PWM$_4$ from $V_{\text{CC}}$ to $V_{\text{out}}$ to reliably drive the high-side PMOS. Resistors ($R_{dt1,2}$) and capacitors ($C_{dt1,2}$) in Fig. 12 are used to generate and control dead time. Four transistors are directly driven by logic devices, without additional gate drivers.

### *B. Controller Design and Implementation of P&O*

The dual-resistor input current sensing circuit and proportional, differential, and integral operation circuit designed in this article are shown in Fig. 13. To avoid using dual power supply, bias voltage of $V_{\text{CC}}/2$ or $V_{\text{out}}/2$ is added to all signal processing circuits in this article. When $v_{\text{ref}}$ is positive, T$_2$ is ON, $R_{s2}$ is grounded and used for sampling the input current. When $v_{\text{ref}}$ is negative, T$_1$ is ON, $R_{s1}$ is grounded and used for sampling. In this way, there is almost no common-mode voltage on sampling resistors, which reduces the requirement for common-mode rejection ratio of the differential amplifier and helps reduce power consumption.

The proportional, integral, and differential circuits with variable gains are realized by the amplifier with digital potentiometer (MAX5424). The potentiometer is controlled by the MCU through serial peripheral interface (SPI). The specific gains are given in (19)–(22). Analog switch (TSA3159A) is used to switch between integral and differential operations, which is also controlled by the MCU.

Output power sensing circuit is shown in Fig. 14. Output voltage ($V_{\text{out}}$) is sampled through a megohm-level resistive voltage divider by the analog-to-digital converter (ADC) of the MCU. Output current ($I_{\text{out}}$) is amplified and extracted by a second-order low-pass filter with a cutoff frequency of 3 Hz. Output power ($P_{\text{out}}$) is obtained by multiplying $V_{\text{out}}$ and $I_{\text{out}}$ in the MCU, which will be used to determine the direction of perturbation.

The SPI and ADC modules only require a very short operation time, enabling the MCU to sleep most of the time. There are only few microwatts of static power consumption of the MCU under sleep mode [24], which can greatly reduce the power consumption of the controller.

The flowchart of the proposed impedance circle-based P&O method is shown in Fig. 15. The algorithm consists of two P&Os

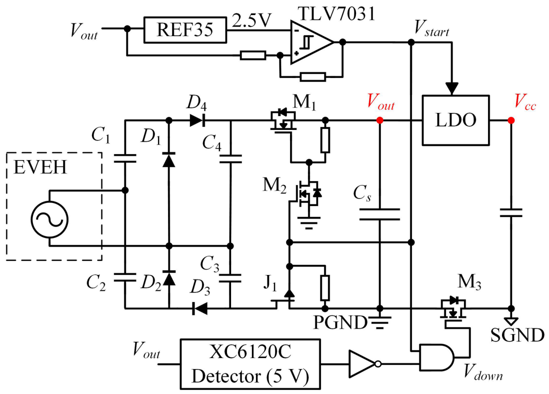

Fig. 16. Start-up circuit and shutdown circuit.

with different time-scale. The short time-scale P&O only needs to perturb $\varphi_L$ to adapt to the change in vibration frequency. Long time-scale and dual-variable P&O is used to find the optimal $R'_m$ value, once every few days or even months. It is designed to execute 20 short time-scale P&O with alternately perturbing $\varphi_L$ and $R'_m$ every four intervals [20]. This dual time-scale P&O method simplifies the process of finding the matched impedance. Only one variable needs to be perturbed in most of the time, highlighted in the red dotted box in Fig. 15, which helps to perform a fast impedance matching with high accuracy.

### C. Start-Up and Shutdown Circuit

Start-up and shutdown circuit are designed as shown in Fig. 16. The normally ON depletion N-MOS ($M_1$) and J-FET ($J_1$) are used to maintain the path during the start-up process. $M_2$ is used to pull the gate of $M_1$ low to turn OFF $M_1$. $M_3$ is adopted to control the connection of power GND (PGND) and signal GND (SGND). The control circuits are all connected to SGND. Turning OFF $M_3$ can stop the control circuit from working.

During the cold start stage, the EVEH charges the supercapacitor through a quadruple voltage multiplier. $M_3$ is turned OFF to prevent unwanted working.

The voltage reference module (REF35) is supplied by $V_{\text{out}}$ to generate a 2.5-V reference. When $V_{\text{out}}$ reaches 2.6 V, the output of hysteresis comparator ($V_{\text{start}}$) turns high to turn OFF $J_1$ and $M_1$, turn ON $M_3$. Low dropout (LDO) linear regulator is also enabled. The impedance controller starts to work. Two supply voltages ($V_{\text{out}}$ and $V_{\text{CC}}$) are provided in this stage: $V_{\text{out}}$ is the unregulated output voltage to power PMOS drivers and analog switches to avoid latch-up; $V_{\text{CC}}$ is kept at 2.5 V to power MCU and other analog devices.

When the supercapacitor is fully charged, the voltage detector (XC6120C) generates a shutdown signal ($V_{\text{down}}$). $M_3$ is turned OFF to disconnect SGND and PGND. The ac-dc converter stops working.

## V. EXPERIMENTAL RESULTS

### A. Prototype Design

A cylinder-type EVEH is adopted to verify the automatic impedance matching system proposed in this article, shown in Fig. 17. The outer diameter and thickness of this prototype is 42 and 31 mm, respectively. The cylindrical NdFeB magnet has a radius of 10 and a thickness of 12 mm. The winding positions for coils are at both upper and bottom surfaces of the cylindrical magnet for the larger radial magnetic flux density [31]. Relative movement between magnet and coil is generated via two planar springs. The induced electromotive force is generated in the coil by Faraday's law. Resonant frequency of this device is at 89.0 Hz. The detail parameters of the EVEH are summarized in Table I.

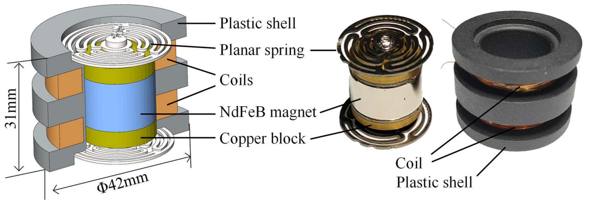

Fig. 17. Structure of the cylinder-type EVEH.

TABLE I
PARAMETERS OF THE CYLINDER-TYPE EVEH

| Parameter | Value |
|---|---|
| Mechanical damping coefficient, $c_{\text{mech}}$ | 0.345 N·s/m |
| Mass, $m$ | 64.6 g |
| Resonant frequency, $\omega_n$ | 89*2π rad/s |
| Electromechanical coupling coefficient, $\theta$ | 4.67 T·m |
| Coil resistance, $R_c$ | 6.7 Ω |
| Coil inductance, $L_c$ | 1.03 mH |
| Settling time, $t_{\text{mech}}$ ($\varepsilon_t$=1%) | Less than 1.95 s |
| Maximum output power at resonance, $P_{\max}$ | 12.3 mW at 3 m/s$^2$ |

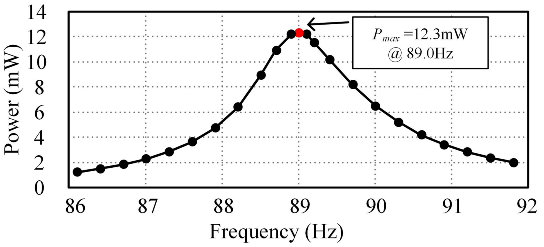

Fig. 18. Output power of the designed EVEH under resistance matching at different vibration frequencies, tested with fixed acceleration amplitude of 3 m/s$^2$.

The resistance matched output power of the designed cylinder-type EVEH is first tested under different frequencies with fixed excitation vibration acceleration amplitude of 3 m/s$^2$, as shown in Fig. 18. At the resonant frequency of 89.0 Hz, the maximum output power of the EVEH reaches 12.3 mW with a 70-Ω resistor load. The power density of the EVEH prototype reaches 3.18 mW/cm$^3$/g$^2$, where g is gravitational acceleration.

The inductor-less automatic impedance matching system is implemented on a circular printed circuit board (PCB) as shown in Fig. 19, with diameter of 39 mm. Two GaN HEMTs (EPC2037) and two PMOS (PMH950) are adopted as power transistors. The key component parameters are listed in Table II.

The fully integrated self-powered EVEH system is shown in Fig. 20(a), with an outer diameter and height of 43 and 42 mm, respectively. The test bench with vibration shaker is shown in Fig. 20(b).

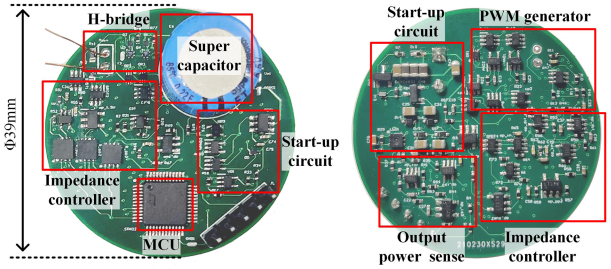

Fig. 19. Circular PCB prototype of the inductor-less automatic impedance matching system.

TABLE II
KEY PARAMETERS OF THE DESIGNED PCB PROTOTYPE

| Parameter | Value |
|---|---|
| Power supply voltage, $V_{CC}$ | 2.5 V |
| Start-up voltage, $V_{\text{out\_start}}$ | 2.6 V |
| Shut-down voltage, $V_{\text{out\_down}}$ | 5.0 V |
| Lower Transistors, $T_{1,2}$ | EPC2037 ($Q_g$=115 pC) |
| Higher Transistors, $T_{3,4}$ | PMH950 ($Q_g$=290 pC) |
| Depletion N-MOS, $M_1$ | BSS139 |
| Enhancement N-MOS, $M_{2,3}$ | PMZ130 |
| J-FET, $J_1$ | MMBFJ177 |
| Diode, $D_{1\sim4}$ | 1PS79SB30 |
| Super-capacitor, $C_s$ | FT0H224ZF (220 mF) |
| Sampling resistors, $R_{s1,s2,s3}$ | 0.5 Ω |
| Microcontroller | STM32L433CC (1.3 μA in stop mode) |
| Settling time, $t_{\text{cir}}$, ($\varepsilon_i$=1%) | 0.47 s |

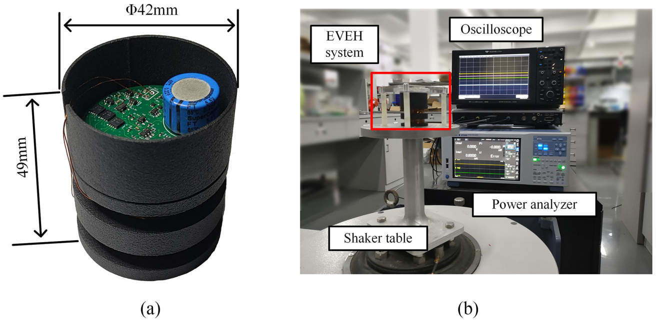

(a)

(b)

Fig. 20. (a) Compact integrated impedance matching EVEH system. (b) Test bench.

### B. Steady-State Performance of the System

The steady-state performances of the designed impedance matching system under different frequencies are tested in this section. A 3-V dc regulated power source is adopted in parallel with the supercapacitor to maintain $V_{\text{out}}$ fixed. The vibration acceleration amplitude is selected as 3 m/s$^2$. Waveforms of two reference signals ($v_{\text{ref}}$ and $-v_{\text{ref}}$), triangular wave ($v_{\text{tri}}$), and drive signal PWM$_1$ are shown in Fig. 21. It can be seen that the frequency of $v_{\text{tri}}$ is 26.7 kHz. Under bipolar double-frequency modulation, frequency of PWM signals is 53.4 kHz. The measured four PWM signals are shown in Fig. 22. In half vibration cycle, the states of two transistors (T$_1$, T$_3$ or T$_2$, T$_4$) are always remain unchanged. This working mode can reduce switching loss and driving loss of transistors.

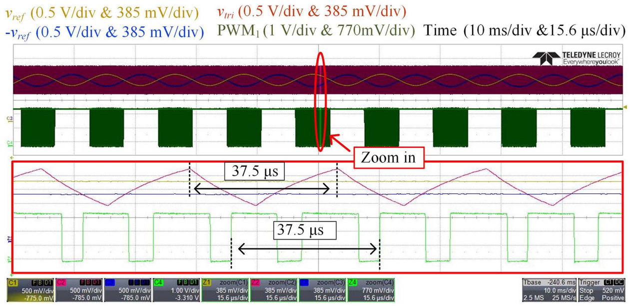

Fig. 21. Waveforms of two reference signals ($v_{\text{ref}}$ and $-v_{\text{ref}}$), triangular wave ($v_{\text{tri}}$), and PWM$_1$.

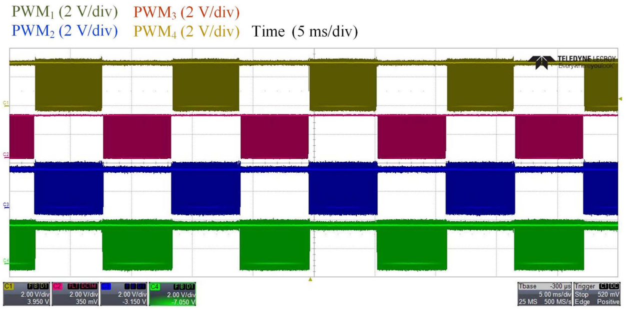

Fig. 22. Measured waveforms of four PWM signals.

Changing the gain coefficients of proportional, integral, and differential can change the phase and amplitude of $v_{\text{ref}}$. Thus, the equivalent impedance of the H-bridge converter can be controlled as inductive, resistive, or capacitive to realize impedance matching at different load central angle $\varphi_L$. Fig. 23(a)–(c) shows the waveforms of $V_{\text{out}}$, $v_{\text{ref}}$, and $i_{\text{EH}}$ when $\varphi_L$ is 90°, 0°, and $-90°$, respectively. The vibration frequency is kept at 89 Hz in this test. The MCU is working in debug mode so as to change $\varphi_L$ arbitrarily. The output voltage of the EVEH ($v_{\text{EH}}$) can be considered to be in phase with $v_{\text{ref}}$. It can be seen that the phases of $i_{\text{EH}}$ and $v_{\text{EH}}$ in the three figures differ by $-39.8°$, 0°, and 39.8°, illustrating that the input impedance of the H-bridge can be controlled as inductive, resistive, and capacitive, respectively.

The premeasured $R_c$ and $R_m$ are 6.3 and 63.7 Ω. According to the method in Section III, the impedance circle and step sizes can be pregenerated in the MCU. $t_{\text{mech}}$ can be calculate by (25) as less than 1.95 s and $t_{\text{cir}}$ is designed as 0.47 s. Thus, the time interval ($\Delta t_{\text{P\&O}}$) of $\varphi_L$ perturbation is set to 3 s in the experiment. In most of the time, the proposed dual-time-scale P&O method only perturbs $\varphi_L$. The corresponding Gain$_{P,I,D}$ will be controlled through (19)–(22) by the MCU that wakes up once every 3 s. Fig. 24 shows the steady-state waveform of $i_{\text{EH}}$, average output current ($\bar{I}_{\text{out}}$), and the determined $\varphi_L$ under vibration of 3 m/s$^2$ at 88.3 Hz and $V_{\text{out}}$ of 3 V. $\bar{I}_{\text{out}}$ is the filtered output current of the converter by the second-order low-pass filter with a cutoff frequency of 3 Hz. $\varphi_L$ is a parameter in the calculation process of the MCU and cannot be directly measured by the oscilloscope. It is plotted manually on the screenshot of the oscilloscope by reading the memory of the MCU after the

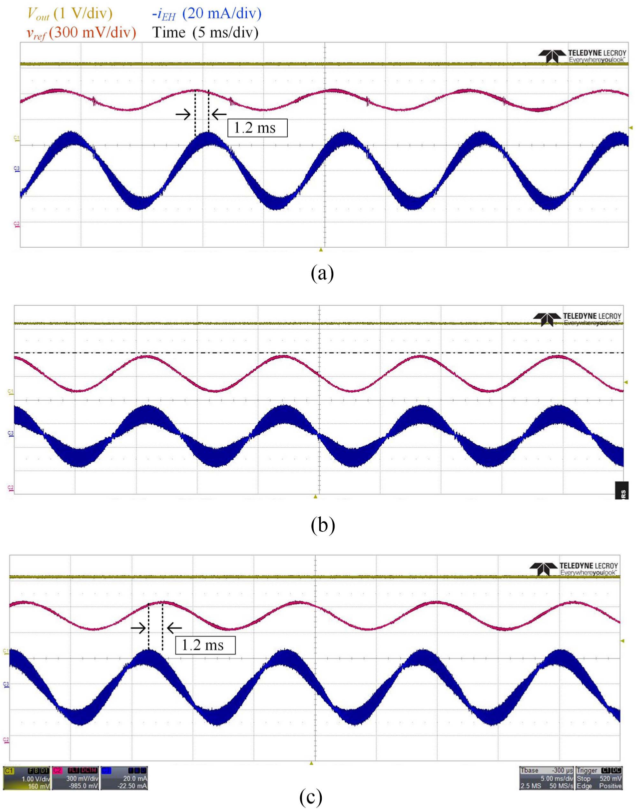

(a)

(b)

(c)

Fig. 23. Measured waveforms of $V_{\text{out}}$, $v_{\text{ref}}$, and $i_{\text{EH}}$ when the equivalent impedance of the H-bridge converter is (a) $\varphi_L = 90°$ inductive, (b) $\varphi_L = 0°$ resistive, and (c) $\varphi_L = -90°$ capacitive.

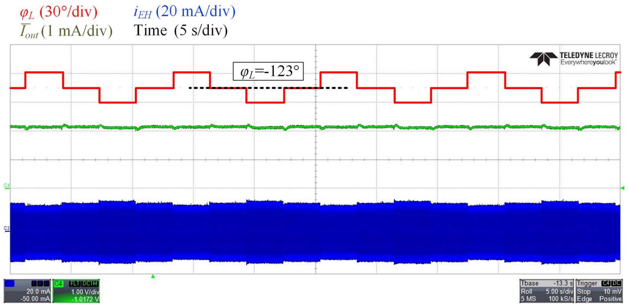

Fig. 24. Steady-state waveform of $i_{\text{EH}}$, average output current ($\bar{I}_{\text{out}}$), and the determined $\varphi_L$ under vibration of 3 m/s$^2$ at 88.3 Hz and $V_{\text{out}}$ of 3 V.

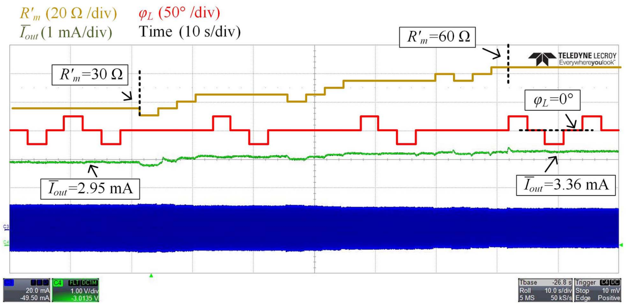

Fig. 25. Process of $R'_m$ determination, tested under vibration of 3 m/s$^2$ at 89 Hz and $V_{\text{out}}$ of 3 V.

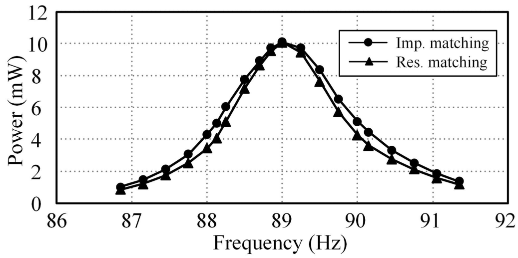

Fig. 26. Output power of impedance matching and resistance matching system, tested under acceleration of 3m/s$^2$ and $V_{\text{out}}$ of 3 V.

experiment test. It can be seen that the system operates in a stable steady trilevel work condition with $\varphi_L$ fluctuating among $-107°$, $-123°$, and $-138°$ every 3 s.

Fig. 25 shows the process of the determination of $R'_m$, where $R'_m$ and $\varphi_L$ are plotted by reading the memory of the MCU. Initial $R'_m$ value is preset to 30 Ω with a large deviation from real value for testing. The step size of $R'_m$ perturbation is set to be 5 Ω. It can be seen that $R'_m$ and $\varphi_L$ are perturbed alternately and toggled every four intervals. After 20 intervals (one minute), $R'_m$ changes from 30 to 60 Ω. The average output current rises from 2.95 to 3.36 mA and the output power rises from 8.85 to 10.08 mW. In practical applications, $R_m$ of the EVEH changes very slowly. This process may be carried out every few days or months.

### *C. Efficiency and Power Overheads*

Efficiency and power overheads of the proposed self-powered impedance matching system are tested. Fig. 26 shows the output power of the complex impedance matching system at different frequencies, under the 3-V dc regulated load and excitation acceleration amplitude of 3 m/s$^2$. For comparison, an optimal purely resistance matching is also implemented in the MCU under the same condition. At nonresonant frequencies, the impedance matching system will deliver more output power than the resistance matching system.

Define the output power improvement factor of complex impedance matching to resistance matching as

$$\eta_i = \frac{P_{\text{out\_imp}} - P_{\text{out\_res}}}{P_{\text{out\_res}}} \tag{26}$$

where $P_{\text{out\_imp}}$ and $P_{\text{out\_res}}$ are output power of the converter under complex impedance matching and resistance matching, respectively. Fig. 27 shows the output power improvement factor under different frequencies. It can be seen that 25% and 23% output power improvements can be obtained at 88.0 and 90.2 Hz, respectively. Additionally, to illustrate the accuracy of impedance circle matching, the proportional, integral, and differential gains are manually adjusted to find the optimal output power. The results are also plotted in Fig. 27 for comparison. It can be seen that the P&O matching by impedance circle has almost the same output power improvement with the manual

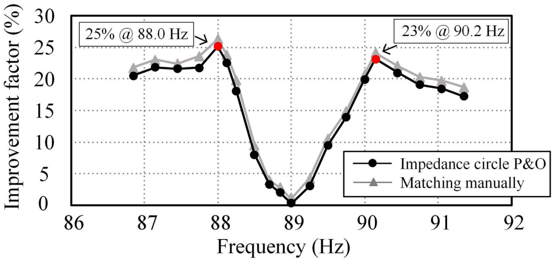

Fig. 27. Output power improvement factor at different frequencies. Tested under acceleration of 3m/s$^2$.

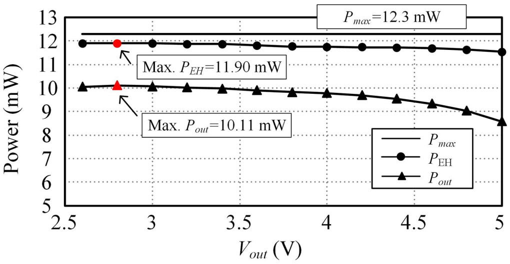

Fig. 28. Measured output power ($P_{\text{out}}$) of the converter and output power of the EVEH ($P_{\text{EH}}$) under different $V_{\text{out}}$, tested with acceleration amplitude of 3 m/s$^2$ at 89 Hz.

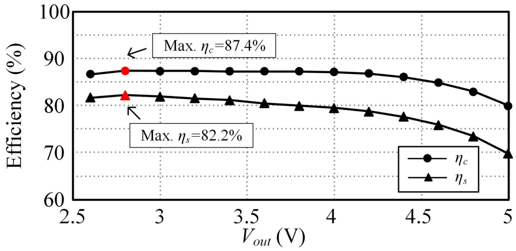

Fig. 29. Overall efficiency of the whole EVEH system and power conversion efficiency of the H-bridge converter under different $V_{\text{out}}$, tested with acceleration of 3 m/s$^2$ at 89 Hz.

adjustment, and the error is within 3%. The correctness of the proposed approach is proved.

Fig. 28 further shows the measured output power of the converter ($P_{\text{out}}$) and EVEH ($P_{\text{EH}}$) at different $V_{\text{out}}$, tested under acceleration amplitude of 3 m/s$^2$ at 89 Hz. The maximum extractable power ($P_{\text{max}}$) at resonance is also plotted for comparison. When the output voltage is 2.8V, the maximum output power of the converter reaches 10.11 mW, and the EVEH outputs the maximum power of 11.90 mW. Define the overall efficiency of the system as

$$\eta_s = \frac{P_{\text{out}}}{P_{\text{max}}} \tag{27}$$

where $\eta_s$ describes the overall output performance of the entire self-powered module. $\eta_s$ at different $V_{\text{out}}$ is plotted in Fig. 29. The maximum overall efficiency reaches 82.2% at $V_{\text{out}}$ of 2.8 V.

In order to investigate the efficiency of the H-bridge converter alone, an external 5-V dc power supply is adopted to power all of the auxiliary control circuits. Define the power conversion efficiency of the inductor-less boost ac–dc converter as

$$\eta_c = \frac{P_{\text{out\_ex}}}{P_{\text{EH\_ex}}} \tag{28}$$

where $P_{\text{out\_ex}}$ and $P_{\text{EH\_ex}}$ are the output power of the converter and the EVEH under external power supply, respectively. $\eta_c$ at different $V_{\text{out}}$ is also plotted in Fig. 29. It can be seen that the maximum conversion efficiency reaches 87.4% at $V_{\text{out}}$ of 2.8 V.

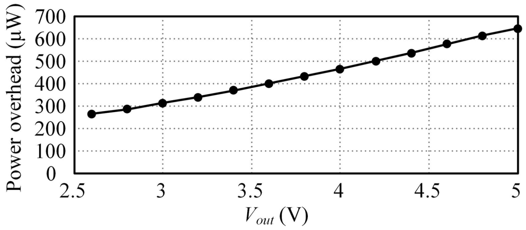

Fig. 30. Power overheads under different $V_{\text{out}}$.

TABLE III
POWER LOSS DISTRIBUTION AT OUTPUT VOLTAGE OF 2.8 V

| Components | | Loss (mW) |
|---|---|---|
| Control loss<br>(0.29 mW) | MCU | 0.01 |
| | Signal processing circuits, static loss | 0.17 |
| | Signal processing circuits, dynamic loss | 0.02 |
| | Driving loss | 0.06 |
| | LDO loss | 0.03 |
| Converter loss<br>(1.50 mW) | Sampling resistor loss | 0.19 |
| | Conduction loss of H-bridge | 0.59 |
| | Other losses and switching loss of H-bridge | 0.72 |
| Total loss | | 1.79 |

Power overhead ($P_{\text{overhead}}$) is defined to evaluate the extra power consumptions to realize the EVEH system self-powering. The current flow from PGND to SGND ($I_{\text{SGND}}$) is measured to calculate $P_{\text{overhead}}$, as

$$P_{\text{overhead}} = V_{\text{out}} I_{\text{SGND}}. \tag{29}$$

The measured result of power overheads under different $V_{\text{out}}$ is plotted in Fig. 30. During the charging process from 2.6 to 5 V, power overheads change from 260 to 640 $\mu$W, which include the static and dynamic power consumption of all signal processing devices, the power consumption of the MCU, and the driving loss of transistors.

A detailed power loss distribution is shown in Table III. It is analyzed at $U_{\text{out}}$ of 2.8 V, vibration frequency of 89 Hz, and amplitude of 3 m/s$^2$. Control circuit and converter consume 0.29 and 1.50 mW, respectively. The power consumption of the MCU is about 2 mW in working mode [24]. But it is active for only several milliseconds for every 3 s. This results in an average power consumption of about 10 $\mu$W, which can greatly reduce the power consumption of the control circuit. The maximum output power of the whole module is 10.11mW. The overall volume of the module is 67.9 cm$^3$. Thus, the corresponding maximum power density of the self-power EVEH module reaches 1.65 mW/cm$^3$/g$^2$.

TABLE IV
COMPARISON WITH OTHER IMPEDANCE MATCHING TECHNIQUES IN ENERGY HARVESTING

| Works | Impedance matching type | Impedance determination method | External sensors | Self-powered | Max. overall efficiency |
|---|---|---|---|---|---|
| [9] | Resistance matching | Given in advance | Auxiliary coils | Yes | 77.6% |
| [11] | Resistance matching | Sigle-variable P&O | No | Yes | 69.0% |
| [17] | Complex impedance matching | Given in advance | Tacho-generator | No | N/A |
| [19] | Complex impedance matching | Given in advance | No | Yes | 71.0% |
| [20] | Complex impedance matching | Dual-variable P&O | No | No | 72.1% (Without control loss) |
| [21] | Complex impedance matching | Dual-variable O&O | Piezo-sensor | No | 55.6% (Without control loss) |
| [23] | Complex impedance matching | P&O and observing critical state | No | No | N/A |
| **This work** | **Complex impedance matching** | **Dual-variable P&O with dual time-scale** | **No** | **Yes** | **82.2%** |

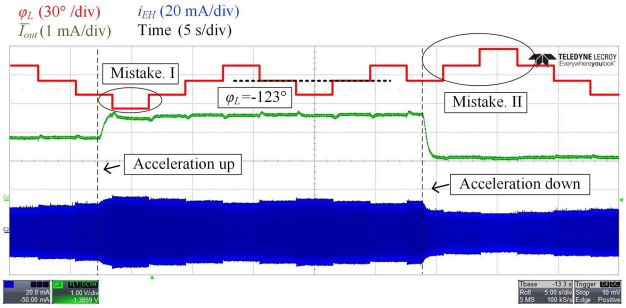

Fig. 31. Determined $\varphi_L$, $\bar{I}_{\text{out}}$, and $i_{\text{EH}}$ when excitation acceleration amplitude rises from 3 to 3.5 m/s$^2$ and down to 2.5 m/s$^2$, test with fixed vibration frequency of 89 Hz and $V_{\text{out}}$ of 3 V.

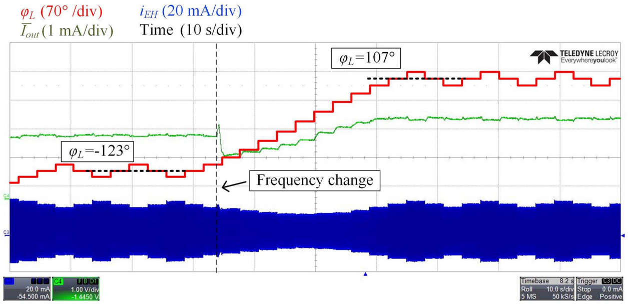

Fig. 32. Determined $\varphi_L$, $\bar{I}_{\text{out}}$, and $i_{\text{EH}}$ when vibration frequency changes from 88.3 to 89.6 Hz, test with fixed acceleration amplitude of 3 m/s$^2$ and $V_{\text{out}}$ of 3 V.

## C. Transient Response to the Change of Acceleration and Frequency

Transient response performance of the designed system is investigated in this section. Fig. 31 shows the determined $\varphi_L$, $\bar{I}_{\text{out}}$, and $i_{\text{EH}}$ when excitation acceleration changes from 3 to 3.5 m/s$^2$, and then, down to 2.5 m/s$^2$, tested at fixed vibration frequency of 89 Hz. The suddenly changed output power will lead to misjudgment of $\varphi_L$ perturbation. After one or two wrong perturbations (Mistakes I and II in Fig. 30), $\varphi_L$ will return to the new optimal trilevel steady-state working mode, which shows that the designed system has strong stability and can automatically find the optimal $\varphi_L$.

To demonstrate the transient response of frequency changes, the vibration frequency is suddenly changed from 88.3 to 89.6 Hz. Fig. 32 shows the determined $\varphi_L$, $\bar{I}_{\text{out}}$, and $i_{\text{EH}}$ in this process, tested with fixed $V_{\text{out}}$ of 3 V. It can be seen when the frequency changes, the output power drops due to the impedance change of the EVEH. After 12 perturbations, $\varphi_L$ stabilizes from –123° to 107°, which realizes the correct measurement of impedance and gradually increases the output power.

## D. Full Charging Performance of the Proposed Self-Powered EVEH System

The overall charging performance to a 220-mF supercapacitor from zero-voltage to full voltage of 5 V is investigated, under an acceleration amplitude of 3 m/s$^2$ and frequency of 89 Hz. The waveform of $V_{\text{out}}$, $i_{\text{EH}}$, $V_{\text{start}}$, and $V_{\text{down}}$ during the charging process is shown in Fig. 33. In the start-up stage, the EVEH charges the supercapacitor through a voltage multiplier. After 171 s, $V_{\text{out}}$ reaches 2.6 V, $U_{\text{star}}$ is high to cutoff voltage multiplier and the impedance controller starts working. After 269 s, $V_{\text{out}}$ reaches 5 V and the system stop charging. The average power for the charging process can be calculated by

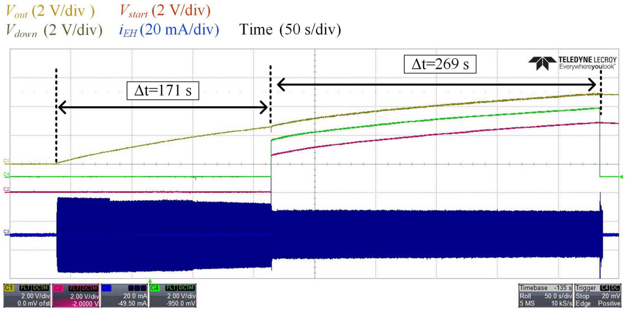

Fig. 33. Charging process of a 220-mF supercapacitor, tested with acceleration amplitude of 3 m/s$^2$ at 89 Hz.

$$P_{\text{av}} = \frac{C_s \left(V^2_{\text{out\_start}} - V^2_{\text{out\_stop}}\right)}{2t_{\text{charge}}} \tag{30}$$

where $t_{\text{charge}}$ is the time to charge $C_s$ from $V_{\text{out\_start}}$ to $V_{\text{out\_stop}}$. $P_{\text{av}}$ is calculated as 7.46 mW during the charge process from 2.6 to 5 V. This is slightly lower than the steady state overall efficiency in Fig. 26, due to the large equivalent series resistance loss of the supercapacitor.

### *E. Comparison With Other Works*

A comparison with other impedance matching techniques in an energy harvesting system is shown in Table IV. Compared with the only resistance matching works [9], [11], the complex impedance matching technique in this article increases the output power at the nonresonant frequencies, which also can be proved by the experimental results in Fig. 26. Compared with other complex impedance matching works, this article is the first to present a self-powered and compact automatic impedance matching EVEH system. Besides, the proposed dual-time scale P&O method has a better response speed and accuracy to determine the complex impedance.

## VI. CONCLUSION

This article is the first to present a high-efficiency and compact automatic complex impedance matching EVEH system for increasing the output power at nonresonant vibration frequencies. The output characteristic of the EVEH under different frequencies is firstly analyzed to illustrate that the impedance is distributed on a circle. A fast and accurate impedance circle-based P&O method that perturbs the angle and diameter with dual time-scale is proposed to determine the complex impedance of the EVEH. In most of the time, only the central angle is perturbed to determine the complex impedance, which helps to improve the response speed and accuracy of the P&O method. Additionally, an automatic low-power impedance matching system is designed for implementing complex impedance control. A compact cylinder-type EVEH prototype is designed in this article to verify the proposed impedance matching method. Experiments show that the designed system can realize complex impedance matching control stably and quickly. It can effectively increase the output power of the EVEH at any nonresonant frequencies. The maximum improvement reaches 25% compared to the traditional resistance matching schemes. Under the excitation acceleration of 3 m/s$^2$, the system generates the maximum power of 10.11 mW with the overall system efficiency of 82.2%. The power density of the whole self-powered EVEH module reaches 1.65 mW/cm$^3$/g$^2$.

## REFERENCES

[1] L. Rome, L. Flynn, and E. Goldman, “Generating electricity while walking with loads,” *Science*, vol. 309, pp. 1725–1728, Sep. 2005, doi: 10.1126/science.1111063.

[2] Y. Ikawa, T. Kobayashi, and T. Matsubara, “Biomechanical energy harvester with continuous variable transmission: Prototyping and preliminary evaluation,” in *Proc. IEEE/ASME Int. Conf. Adv. Intell. Mechatronics*, 2018, pp. 1045–1050, doi: 10.1109/AIM.2018.8452395.

[3] C Wei and X Jing, “A comprehensive review on vibration energy harvesting: Modelling and realization,” *Renewable Sustain. Energy Rev.*, vol. 74, pp. 1–18, Jul. 2017, doi: 10.1016/j.rser.2017.01.073.

[4] H. Xiao, H. Peng, and J. Yuan, “A coil connection switching strategy for maximum power delivery in electromagnetic vibration energy harvesting system,” in *Proc. IEEE Energy Convers. Congr. Expo.*, 2021, pp. 5867–5872, doi: 10.1109/ECCE47101.2021.9595410.

[5] Z. Xie, L. Teng, H. Wang, Y. Liu, M. Fu, and J. Liang, “A self-powered synchronous switch energy extraction circuit for electromagnetic energy harvesting enhancement,” *IEEE Trans. Power Electron.*, vol. 38, no. 8, pp. 9972–9982, Aug. 2023, doi: 10.1109/TPEL.2023.3272586.

[6] J. Leicht, D. Maurath, and Y. Manoli, “Autonomous and self-starting efficient micro energy harvesting interface with adaptive MPPT, buffer monitoring, and voltage stabilization,” in *Proc. Eur. Conf. Solid-State Circuits*, 2012, pp. 101–104, doi: 10.1109/ESSCIRC.2012.6341266.

[7] J. C. Rodriguez, V. Nico, and J. Punch, “Powering wireless sensor nodes for industrial IoT applications using vibration energy harvesting,” in *Proc. IEEE 5th World Forum Internet Things*, 2019, pp. 392–397, doi: 10.1109/WF-IoT.2019.8767352.

[8] G. D. Szarka, S. G. Burrow, and B. H. Stark, “Ultralow power, fully autonomous boost rectifier for electromagnetic energy harvesters,” *IEEE Trans. Power Electron.*, vol. 28, no. 7, pp. 3353–3362, Jul. 2013, doi: 10.1109/TPEL.2012.2219594.

[9] H. Xiao, H. Peng, X. Liu, and H. Sun, “Fully self-powered inductorless electromagnetic vibration energy harvesting system using auxiliary coils for hysteresis current MPPT control,” *IEEE Trans. Power Electron.*, vol. 37, no. 11, pp. 13192–13204, Nov. 2022, doi: 10.1109/TPEL.2022.3182155.

[10] J. Chen, H. Peng, Z. Feng, and Y. Kang, “A GaN BCM AC–DC converter for sub-1 V electromagnetic energy harvesting with enhanced output power,” *IEEE Trans. Power Electron.*, vol. 36, no. 8, pp. 9285–9299, Aug. 2021, doi: 10.1109/TPEL.2020.3048195.

[11] G. D. Szarka, S. G. Burrow, P. P. Proynov, and B. H. Stark, “Maximum power transfer tracking for ultralow-power electromagnetic energy harvesters,” *IEEE Trans. Power Electron.*, vol. 29, no. 1, pp. 201–212, Jan. 2014, doi: 10.1109/TPEL.2013.2251427.

[12] L. Costanzo, A. L. Schiavo, and M. Vitelli, “Design guidelines for the perturb and observe technique for electromagnetic vibration energy harvesters feeding bridge rectifiers,” *IEEE Trans. Ind. Appl.*, vol. 55, no. 5, pp. 5089–5098, Sept.-Oct. 2019, doi: 10.1109/TIA.2019.2923162.

[13] S. Chang, “Harvesting energy from non-ideal vibrations,” Ph.D. thesis, Massachusetts Inst. Technol., Cambridge, MA, USA, 2013. [Online]. Available: https://dspace.mit.edu/handle/1721.1/82346

[14] W. Choi, H. Kim, C. Park, and B. Lee, “Study on electromagnetic energy transducer in ambient vibration,” *IET Power Electron.*, vol. 11, no. 12, pp. 1983–1990, Oct. 2018, doi: 10.1049/iet-pel.2017.0886.

[15] A. Cammarano, S. G. Burrow, D. A. W. Barton, A. Carrella, and L. R. Clare, “Tuning a resonant energy harvester using a generalized electrical load,” *J. Smart Mater. Struct.*, vol. 19, no. 5, Mar. 2010, Art. no. 055003, doi: 10.1088/0964-1726/19/5/055003.

[16] D. Zhu, S. Roberts, T. Mouille, M. J. Tudor, and S. Beeby, “General model with experimental validation of electrical resonant frequency tuning of electromagnetic vibration energy harvesters,” *J. Smart Mater. Struct.*, vol. 21, no. 10, Sep. 2012, Art. no. 105039.

[17] P. D. Mitcheson, T. T. Toh, K. H. Wong, S. G. Burrow, and A. S. Holmes, “Tuning the resonant frequency and damping of an electromagnetic energy harvester using power electronics,” *IEEE Trans. Circuits Syst. II*, vol. 58, no. 12, pp. 792–796, Dec. 2011, doi: 10.1109/TCSII.2011.2173966.

[18] J. A. Bowden, S. G. Burrow, A. Cammarano, L. R. Clare, and P. D. Mitcheson, “Switched-mode load impedance synthesis to parametrically tune electromagnetic vibration energy harvesters,” *IEEE/ASME Trans. Mechatronics*, vol. 20, no. 2, pp. 603–610, Apr. 2015, doi: 10.1109/TMECH.2014.2325825.

[19] U. Radhakrishna et al., “A low-power integrated power converter for an electromagnetic vibration energy harvester with 150 mV-AC cold startup, frequency tuning, and 50 hz AC-to-DC conversion,” in *Proc. IEEE Custom Integr. Circuits Conf.*, 2018, pp. 1–4, doi: 10.1109/CICC.2018.8357079.

[20] Q. Sun, S. Patil, N. Sun, and B. Lehman, “Phase/RMS maximum power point tracking for inductive energy harvesting system,” in *Proc. IEEE Energy Convers. Congr. Expo.*, 2015, pp. 408–413.

[21] L. Costanzo, A. Lo Schiavo, and M. Vitelli, “Active interface for piezoelectric harvesters based on multi-variable maximum power point tracking,” *IEEE Trans. Circuits Syst. I*, vol. 67, no. 7, pp. 2503–2515, Jul. 2020, doi: 10.1109/TCSI.2020.2977495.

[22] K. H. K. Tse and H. S. H. Chung, “Maximum power point tracker for electromagnetic energy harvesting system,” in *Proc. IEEE Energy Convers. Congr. Expo.*, 2017, pp. 5515–5522, doi: 10.1109/ECCE.2017.8096920.

[23] K. H. -k. Tse and H. S. -h. Chung, “MPPT for electromagnetic energy harvesters having nonnegligible output reactance operating under slow-varying conditions,” *IEEE Trans. Power Electron.*, vol. 35, no. 7, pp. 7110–7122, Jul. 2020, doi: 10.1109/TPEL.2019.2959625.

[24] *STM32L433CC. Datasheet*, STMicroelectronics, May 2021. [Online]. Available: https://www.st.com/zh/microcontrollers-microprocessors/stm32l433cc.html

[25] *PIC12(L)F1571/2. Datasheet*, Microchip, Aug. 2015. [Online]. Available: https://ww1.microchip.com/downloads/aemDocuments/documents/OTH/ProductDocuments/DataSheets/40001723D.pdf

[26] N. G. Stephen, “On energy harvesting from ambient vibration,” *J. Sound Vib.*, vol. 293, no. 1–2, pp. 409–425, May 2006, doi: 10.1016/j.jsv.2005.10.003.

[27] C. B. Williams et al., “Development of an electromagnetic micro-generator,” *IEE Proc.—Circuits, Devices Syst.*, vol. 148, no. 6, pp. 337–342, 2001, doi: 10.1049/ip-cds:20010525.

[28] C. Lenk et al., “Neuromorphic acoustic sensing using an adaptive microelectromechanical cochlea with integrated feedback,” *Nature Electron.*, vol. 6, pp. 370–380, 2023, doi: 10.1038/s41928-023-00957-5.

[29] P. Pozsgai, W. Neher, and B. Bertsche, “Models to consider load-sharing in reliability calculation and simulation of systems consisting of mechanical components,” in *Proc. Annu. Rel. Maintainability Symp.*, 2003, pp. 493–499, doi: 10.1109/RAMS.2003.1182038.

[30] L. Costanzo and M. Vitelli, “Resonant electromagnetic vibration harvesters applications: Optimization of P&O MPPT technique parameters,” in *Proc. 13th Int. Conf. Ecological Veh. Renewable Energies*, 2018, pp. 1–8, doi: 10.1109/EVER.2018.8362384.

[31] H. Sun et al., “An optimized design of compact self-powered module based on electromagnetic vibration energy harvester considering engineering feasibility,” *IEEE Trans. Ind. Appl.*, vol. 59, no. 1, pp. 767–778, Feb. 2023, doi: 10.1109/TIA.2022.3209955.

**Hongfei Xiao** (Student Member, IEEE) received the B.S. degree in electrical engineering from the School of Electrical Engineering, Chongqing University, Chongqing, China, in 2020. He is currently working toward the Ph.D. degree in electrical engineering with the School of Electrical and Electronic Engineering, Huazhong University of Science and Technology, Wuhan, China.

His current research interests include vibration energy harvesting and power converters based on wide bandgap devices.

**Han Peng** (Senior Member, IEEE) received the B.S. degree in electrical engineering from Southeast University, Nanjing, China, in 2006, and the Ph.D. degree in electrical engineering from Rensselaer Polytechnic Institute, Troy, NY, USA, in 2011.

From 2011 to 2017, she was a Lead Electrical Engineer with the Global Research Center, General Electric Company, Niskayuna, NY. Since 2018, she has been a Professor with the Huazhong University of Science and Technology, Wuhan, China. She has authored or coauthored more than 60 articles in refereed journals and international conference proceedings. She holds four U.S. patents and four Chinese patents. Her research interests include high-frequency, high-power density power management IC design, high-frequency supply modulators and applications of wide bandgap power devices, energy harvesting, healthcare electronics, electrical aircraft systems, and electric vehicles.

Dr. Peng has been an Associate Editor for the IEEE Transactions on Power Electronics since 2017. She was the Associate Technical Program Chair for IEEE 11th Annual Energy Conversion Congress and Exposition 2019.

**Hanyi Sun** received the B.S. degree in electrical engineering from the Huazhong University of Science and Technology (HUST), Wuhan, China, in 2021, where he is currently working toward the M.S. degree in new energy science and engineering with China-EU Institute for Clean and Renewable Energy.

His research interests include energy harvesting and electrical energy conversion.

**Yidong Zhao** received the B.S. degree in electrical engineering from Qiushi Honor College, Tianjin University, Tianjin, China, in 2022. He is currently working toward the M.S. degree in electrical engineering with the School of Electrical and Electronic Engineering, Huazhong University of Science and Technology, Wuhan, China.

His current research interests include magnetic energy harvesting and electrical energy conversion.

**Xianchao Liu** received the B.S. degree in electrical engineering from the School of Electrical Engineering, Chongqing University, Chongqing, China, in 2020, and the M.S. degree in electrical engineering from the School of Electrical and Electronic Engineering, Huazhong University of Science and Technology, Wuhan, China, in 2023. He is currently working toward the Ph.D. degree in electrical engineering with the University of Tennessee, Knoxville, TN, USA.

His research interests include energy harvesting and high power converters.

**Cheng Jiang** received the B.S. degree in electrical engineering from the Hefei University of Technology, Hefei China, in 2021. She is currently working toward the M.S. degree with the School of Electrical and Electronic Engineering, Huazhong University of Science and Technology, Wuhan, China. Her research includes high-frequency planar transformers and power-signal integrated isolated gate driver.